

Comparison of branch-point detection approaches using a Shack–Hartmann wavefront sensor

Matthew Kalensky^{Ⓞ, a, *} Denis W. Oesch^{Ⓞ, b} Timothy J. Bukowski^{Ⓞ, a}
Kelsey Miller,^a and Darren Getts^a

^aIntegrated Engagement Systems Department, Naval Surface Warfare Center Dahlgren Division,
Dahlgren, Virginia, United States

^bLeidos, Albuquerque, New Mexico, United States

ABSTRACT. Two methods for identifying branch points from Shack–Hartmann wavefront sensor (SHWFS) measurements were studied: the circulation of phase gradients approach and the beam-spread approach. These approaches were tested using a simple optical-vortex model, with wave-optics simulations, and with experimental data. It was found that these two approaches are synergistic regarding their abilities to detect branch points. Specifically, the beam-spread approach works best when the branch point is located toward the center of the SHWFS's lenslet pupil, whereas the circulation of phase gradients approach works best when the branch point is located toward the edge of the SHWFS's lenslet pupil. These behaviors were observed studying the simple optical-vortex model; however, they were further corroborated with the wave-optics and experimental results. The developments presented support researchers studying high scintillation optical-turbulence environments and inform efforts in developing branch-point tolerant reconstruction algorithms.

© The Authors. Published by SPIE under a Creative Commons Attribution 4.0 International License. Distribution or reproduction of this work in whole or in part requires full attribution of the original publication, including its DOI. [DOI: [10.1117/1.OE.62.12.123101](https://doi.org/10.1117/1.OE.62.12.123101)]

Keywords: branch points; optical vortices; wavefront sensing; deep turbulence; atmospheric propagation; Shack–Hartmann wavefront sensor

Paper 20230795G received Aug. 26, 2023; revised Nov. 14, 2023; accepted Nov. 17, 2023; published Dec. 8, 2023.

1 Introduction

When a laser beam propagates through atmospheric turbulence, phase aberrations are imposed onto the beam. These aberrations are caused by propagating through variations in the index-of-refraction that result from temperature fluctuations in the atmosphere. If the atmospheric turbulence is distributed along the beam's propagation path, the accrued phase aberrations will give rise to constructive and destructive interference, referred to as scintillation. The Rytov number is often used to quantify the scintillation imposed onto the laser beam.¹ It is well-documented in the literature that when the Rytov number approaches 0.1, branch points can form. A branch point can be described by a singularity in which both the real and imaginary components of the complex-optical field equal zero.² About this singularity, the phase function of the complex-optical field undergoes a 2π circulation in phase. Furthermore, these branch points form in pairs of opposite helicity with an associated branch cut connecting them.^{3,4} The work of Fried and Vaughn first investigated the problem of branch-point formation caused by propagation through distributed-volume turbulence,⁵ after which researchers began investigating (1) the impact that branch-point formation has on laser-propagation systems^{6–14} and (2) the physical insight that can be gleaned about the atmospheric turbulence environment through which the beam

*Address all correspondence to Matthew Kalensky, matthew.t.kalensky.civ@us.navy.mil

propagated.^{3,4,15–26} These motivations make it advantageous to develop approaches that easily and robustly identify branch points from optical-turbulence measurements.

Due to their great dynamic range and easy operation, the Shack–Hartmann wavefront sensor (SHWFS) is one device commonly used to collect optical-turbulence measurements. An SHWFS is comprised of an array of subaperture lenslets focused onto a camera. The average gradient of the incoming phase aberration over each subaperture in the pupil plane is estimated from irradiance-pattern deflections in the image plane.²⁷ Traditionally, the phase gradients estimated from subaperture irradiance pattern deflections are then used in a least-squares reconstructor to estimate the continuous wavefront aberration.^{28–31} Unfortunately, phase singularities such as branch points are mapped to the null space of a traditional least-squares reconstructor.² In other words, using SHWFS data in a least-squares reconstructor yields accurate estimates of the least-squares or continuous phase; however, the rotational component of phase imposed by branch points is not reconstructed. Various approaches exist for using an SHWFS to identify branch points. The circulation of phase gradients approach is considered the “tried and true” and was first introduced by Fried and Vaughn.⁵ Conversely, a new approach that utilizes a subaperture irradiance pattern beam spread to identify branch points has recently been introduced.^{32,33} Although other approaches exist,^{34–38} these two approaches are the ones emphasized in this paper. Here, the circulation of phase gradients approach and beam-spread approaches are compared using a simple optical-vortex model, wave-optics simulations, and experimental data.

The paper is organized as follows. Section 2 introduces the necessary background information regarding both the circulation of phase gradients and beam-spread approaches. Section 3 discusses the wave-optics simulations and experimental setup. In Sec. 4, the wave-optics and experimental results are presented and discussed. Thereafter, Sec. 5 provides a conclusion for this paper.

2 Background

2.1 Phase-Gradient Circulation Approach

The circulation of phase gradients approach, first introduced by Fried and Vaughn,⁵ is described by

$$\oint_C \nabla \phi \cdot dr = \pm 2\pi(N_+ - N_-), \quad (1)$$

where $\nabla \phi$ are the phase gradients, N_+ is the number of positive branch points contained within the contour, and N_- is the number of negative branch points contained within the contour.^{5,25} If the measured local phase-gradient field can be entirely described by the gradient of the scalar potential, the circulation value calculated from Eq. (1) will be close to zero. However, if the measured phase-gradient field is described by both the gradient of the scalar potential and the curl of the vector potential, the magnitude of the circulation value calculated using Eq. (1) will be appreciably greater than zero, the extent of which depends on the number of branch points that fall within the contour.³⁴ As such, Eq. (1) can be used to identify branch points when the branch point falls within the contour of interest.

2.2 Beam-Spread Approach

Recently, a new approach for identifying branch points from SHWFS measurements was introduced.³² This approach leverages second-moment statistics of the SHWFS’s image-plane irradiance patterns. It was shown that when an optical-phase vortex is located within the pupil of an SHWFS lenslet, the resulting image-plane irradiance pattern exhibits a large degree of beam spreading. This behavior is similar to the pupil-plane phase/image-plane irradiance pattern relationship described by the (1,0) mode of the Laguerre–Gaussian beam.³⁹ By calculating the beam spread for each SHWFS irradiance pattern, branch points can be identified by thresholding to determine which irradiance patterns exhibit sufficient beam spread to qualify for a branch-point identification. The second-moment beam width, also referred to as $D4\sigma$, is one approach to quantify the beam spread.⁴⁰ The equation for $D4\sigma$ in the x dimension is given as

$$D4\sigma_x = 4\sqrt{\frac{\int_{-\infty}^{\infty} \int_{-\infty}^{\infty} I(x, y)(x - \bar{x})^2 dx dy}{\int_{-\infty}^{\infty} \int_{-\infty}^{\infty} I(x, y) dx dy}}, \quad (2)$$

where $I(x, y)$ is the image-plane irradiance pattern and \bar{x} is the centroid location of the beam. A similar equation can be written for $D4\sigma_y$. It is often convenient to report an overall $D4\sigma$, which is given as $D4\sigma = \sqrt{D4\sigma_x^2 + D4\sigma_y^2}$. It is worth noting that to date, this approach cannot determine if more than one branch point falls within a lenslet pupil nor can it determine the helicity of the identifications, unlike the circulation of phase gradients approach described above.

2.3 Simple Optical-Vortex Model

To demonstrate the functionality of both the circulation of phase gradients and beam-spread approaches, we create a complex-optical field with a simple optical vortex, which is shown in Fig. 1(a). For the purposes of this example, we assume uniform illumination over the pupil recognizing, however, that this is not true for turbulence-induced branch points. After creating a complex-optical field with an optical-vortex-phase function, the complex-optical field is applied to an SHWFS model, similar to the ones used in Refs. 27, 32, 41, and 42. The resultant SHWFS image is shown in Fig. 1(b).

Using the resultant SHWFS image, the circulation of phase gradients and beam-spread approaches described above were employed. For the case of the circulation of phase gradients approach, Eq. (1) was applied to 2×2 adjacent subapertures using the x and y slopes calculated from irradiance pattern deflections with the lenslet focal lengths. The circulation value calculated at each 2×2 location was recorded. For the case of the beam-spread approach, $D4\sigma$ was calculated using Eq. (2) for each image-plane irradiance pattern. Here, $D4\sigma$ was normalized by the diffraction-limited spot size for square apertures, $D_{DL} = 2f\lambda/d$, where f is the focal length of the lenslets, λ is the wavelength of the beam, and d is the diameter of the SHWFS lenslet pupils. For the phase shown in Fig. 1(a), the resultant $D4\sigma/D_{DL}$ and circulation of phase gradient calculations as a function of the lenslet location are presented in Figs. 1(c) and 1(d), respectively. Here, we see that both algorithms reported a higher value in the proximity of the singularity.

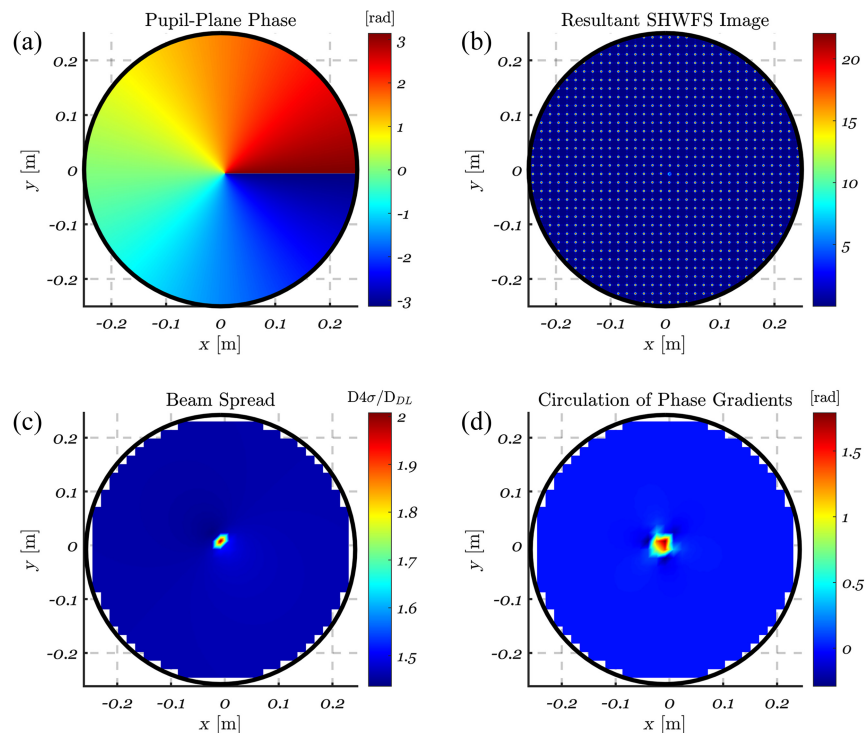


Fig. 1 (a) Pupil-plane phase with simple optical vortex. (b) Resultant SHWFS image. (c) Calculated $D4\sigma/D_{DL}$ from the SHWFS subaperture irradiance patterns. (d) Circulation of phase gradients calculated from the SHWFS slope measurements.

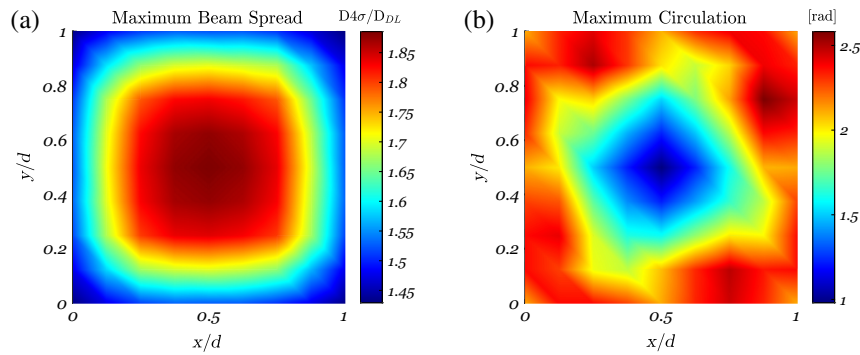


Fig. 2 (a) Maximum $D4\sigma/D_{DL}$ as a function of optical-vortex location. (b) Maximum magnitude of circulation of phase gradients value as a function of optical-vortex location.

Next, to investigate the response of both algorithms as a function of optical-vortex location within the SHWFS lenslet pupils, the location of the optical vortex shown in Fig. 1(a) was moved in both the x - and y -directions across an SHWFS lenslet pupil. At each optical-vortex location, the maximum circulation and $D4\sigma/D_{DL}$ values were recorded. The results of this are shown in Fig. 2.

Figure 2(a) presents the maximum $D4\sigma/D_{DL}$ as a function of the optical-vortex location and Fig. 2(b) presents the maximum magnitude of circulation value as a function of the optical-vortex location. From these results, it is found that the beam-spread approach detects a larger $D4\sigma/D_{DL}$ value when the optical vortex is located toward the middle of the lenslet pupil. (A similar phenomenon was observed in Refs. 41 and 43 for the case of shock-induced-phase aberrations across the SHWFS's lenslet pupils.) The circulation of phase gradients approach tends to detect a larger magnitude circulation value when the optical vortex is located toward the edge of the lenslet pupil. This is an important result as it shows that these two methods for identifying branch points are synergistic. In other words, the beam-spread and circulation of phase gradients approaches have different sensitivities to branch-point location within the lenslet pupils. This behavior is discussed further in Sec. 4.

2.4 Trade-Space Parameterization

It is helpful to introduce the definitions of optical-turbulence parameters prevalent in the literature, namely, Rytov number, \mathcal{R}_{SW} , the atmospheric coherence length, r_0 , and the isoplanatic angle, θ_0 . As described above, the Rytov number is used to describe the strength of scintillation imposed onto the beam. The expression for the spherical-wave Rytov number is described as

$$\mathcal{R}_{SW} = 0.563k^{7/6} \int_0^Z C_n^2(z)(z/Z)^{5/6}(Z-z)^{5/6}dz, \quad (3)$$

where k is the wavenumber of the laser given as $k = 2\pi/\lambda$, Z is the total propagation distance, and C_n^2 is the index-of-refraction structure constant.

The atmospheric coherence length (also referred to as the Fried parameter), r_0 , describes the diameter of an aperture in which ~ 1 rad² of the phase variance is imposed onto the beam. When $D > r_0$, we expect to see beam spreading of the resultant image-plane irradiance pattern. The atmospheric coherence length for a spherical-wave beam is described as

$$r_{0,SW} = \left[0.423k^2 \int_0^Z C_n^2(z)(z/Z)^{5/3}dz \right]^{-3/5}. \quad (4)$$

Finally, the isoplanatic angle, θ_0 , describes the half-angle formed between two points on an object and a distant receiver in which the variance of the phase difference between two beams that propagated from either point on the object to the receiver is ~ 1 rad².¹ The expression for the isoplanatic angle is given as

$$\theta_0 = \left[2.91k^2 \int_0^Z C_n^2(z)(Z-z)^{5/3}dz \right]^{-3/5}. \quad (5)$$

Together, \mathcal{R}_{SW} , $r_{0,SW}$, and θ_0 can be used to parameterize an optical-turbulence environment. These parameters will be referenced throughout the remainder of this paper.

3 Data Collection

This section introduces the wave-optics model used to investigate both the circulation of phase gradients and beam-spread approaches described above as a function of varying turbulence conditions. Because the actual branch-point locations are known in wave-optics simulations, the performance of the approaches described above can be assessed. This section also introduces the experimental setup used to acquire empirical SHWFS data through a distributed-volume, littoral, optical-turbulence environment. The data processing procedures to reduce the experimentally collected SHWFS images are also briefly discussed.

3.1 Wave-Optics Simulations

The wave-optics simulations used here consisted of a point-source beacon that was transmitted through randomly generated phase screens via spherical-wave angular-spectrum propagation. The phase screens were generated using the common approach of filtering Gaussian white noise,^{44–46} and angular-spectrum propagation was accomplished using the well-known split-step beam propagation method.^{44–49} The propagated beacon was received and collimated in a measurement aperture of size, $D = 0.15$ m. For all cases, the beacon wavelength was selected to be $\lambda = 532$ nm. The received complex-optical field was used to identify the “truth” branch-point locations using Eq. (1). Due to the fine resolution of the simulated complex-optical field, this approach provides an excellent method for identifying the known branch-point locations. The received complex-optical field was also applied to an SHWFS model. Here, the resultant SHWFS images were used to calculate both the circulation of phase gradients and beam spread using Eqs. (1) and (2), respectively.

In the simulations used for this work, the phase screens were generated using the von Kármán spectrum, where C_n^2 was varied from 2.27×10^{-15} to $1.33 \times 10^{-13} \text{ m}^{-2/3}$ uniformly distributed over a $Z = 2.5$ km path. The inner scale of turbulence, ℓ_0 , and the outer scale of turbulence, L_0 , were defined to be 1 mm and 100 m, respectively, for all cases. For these simulations, 20 evenly spaced phase screens were used. Each phase screen was $0.6 \times 0.6 \text{ m}^2$ in size and consisted of 2048×2048 points. The SHWFS model consisted of 128×128 square lenslet subapertures across the screen (≈ 32 across the diameter of the receive aperture). As such, each lenslet subaperture had a width of $d = 4.7$ mm. Seventy independent realizations were simulated for each turbulence condition where the Rytov number was varied from $\mathcal{R}_{SW} = 0.1$ to 5.0. A full optical-turbulence parameterization of the wave-optics trade-space can be found in Table 1. As is commonly done, $r_{0,SW}$ was normalized by the diameter of the receiving aperture, $D/r_{0,SW}$, and by the width of the subaperture lenslet of the SHWFS, $d/r_{0,SW}$. In addition, θ_0 was normalized by the diffraction angle as $\theta_0/(\lambda/D)$.

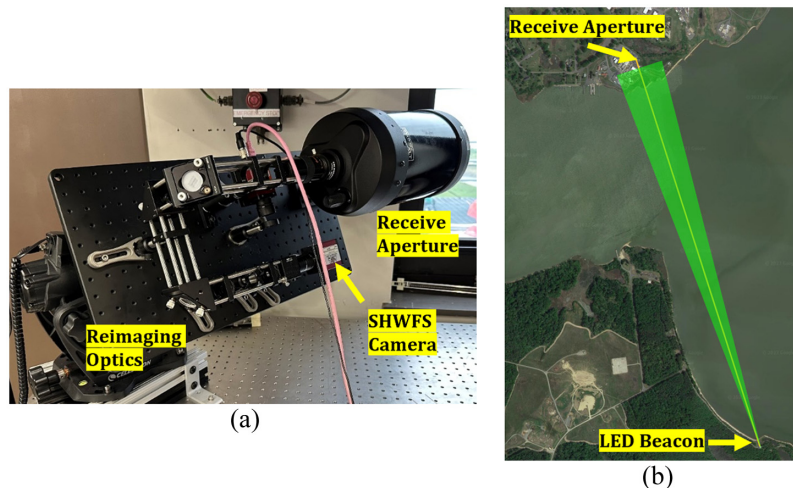
3.2 Experimental Data Collections

3.2.1 Experimental setup

The experimental measurements in this work were collected over the Potomac River Test Range (PRTR) in Dahlgren, Virginia. The PRTR is a littoral test environment and has been previously characterized using various optical-turbulence measurements.^{50,51} For the experiments conducted here, a $\lambda = 532$ nm LED beacon was situated approximately $Z = 2.4$ km away from the receive aperture as shown in Fig. 3(b). The spherical-wave beacon propagated over primarily water and was collected using a Cassegrain–Schmidt telescope with an aperture size of $D = 0.152$ m, a focal length of $f = 1500$ mm, and a central obscuration 56 mm in diameter. A 40 mm lens was used to collimate the beam exiting the telescope, after which, a $4f$ reimaging system comprised of a 175 and a 150 mm lens was used to further demagnify and relay the beam to the SHWFS. The collimated beam entering the SHWFS was 3.4 mm in size, thereby seeing a total system demagnification of 43.75. Prior to entering the SHWFS, a 532 nm line filter was used to limit measurement contamination from ambient light. An Allied Vision GE680C camera was used for the SHWFS assembly. The operating resolution of the camera was 640×480 with each

Table 1 Optical-turbulence parameterization of the wave-optics simulation trade space.

C_n^2 (m ^{-2/3})	\mathcal{R}_{SW}	$D/r_{0,SW}$	$d/r_{0,SW}$	$\theta_0/(\lambda/D)$
2.67×10^{-15}	0.1	3.02	0.09	1.85
5.33×10^{-15}	0.2	4.58	0.14	1.22
8.00×10^{-15}	0.3	5.84	0.18	0.95
1.07×10^{-14}	0.4	6.94	0.22	0.80
1.33×10^{-14}	0.5	7.93	0.25	0.70
1.60×10^{-14}	0.6	8.85	0.28	0.63
1.87×10^{-14}	0.7	9.71	0.30	0.57
2.13×10^{-14}	0.8	10.52	0.33	0.53
2.40×10^{-14}	0.9	11.29	0.35	0.49
2.67×10^{-14}	1.0	12.02	0.38	0.46
2.93×10^{-14}	1.1	12.73	0.40	0.44
3.20×10^{-14}	1.2	13.42	0.42	0.42
3.47×10^{-14}	1.3	14.08	0.44	0.40
3.73×10^{-14}	1.4	14.71	0.46	0.38
4.00×10^{-14}	1.5	15.34	0.48	0.36
4.27×10^{-14}	1.6	15.94	0.50	0.35
4.53×10^{-14}	1.7	16.53	0.52	0.34
4.80×10^{-14}	1.8	17.11	0.53	0.33
5.07×10^{-14}	1.9	17.67	0.55	0.32
5.33×10^{-14}	2.0	18.23	0.57	0.31
6.67×10^{-14}	2.5	20.84	0.65	0.27
8.00×10^{-14}	3.0	23.25	0.73	0.24
9.33×10^{-14}	3.5	25.50	0.80	0.22
1.07×10^{-13}	4.0	27.63	0.86	0.20
1.20×10^{-13}	4.5	29.65	0.93	0.19
1.33×10^{-13}	5.0	31.58	0.99	0.18

**Fig. 3** (a) Experimental optical setup. (b) Satellite map of propagation geometry.

pixel being $7.4 \mu\text{m}$ in size. The SHWFS lenslet array consisted of square subapertures with a pitch of $150 \mu\text{m}$ and focal length of $f = 6.7 \text{ mm}$. The optical system used to collect the incoming light is shown in Fig. 3(a).

3.2.2 Experimental data processing

Traditionally, the images measured with an SHWFS are used to calculate the x and y slopes of the optical-path difference (OPD) aberration over each discrete lenslet location. To do this, the areas of interest (AOIs) need to be identified such that the local displacements of each subaperture image-plane irradiance pattern can be calculated. Typically, averaging collected SHWFS images over a certain number of frames is an effective method for creating a reference image from which the AOIs can be identified. Thresholding is then employed to determine which AOIs to use for subsequent processing. After the AOIs have been identified, the centroid displacements are calculated for each AOI on each frame. Using the centroid displacements and the focal lengths of the subaperture lenslets, the slopes at each discrete subaperture location are calculated. The measured slopes are then used in a least-squares reconstructor to estimate the continuous OPD(x, y, t). This OPD(x, y, t) is converted to a least-squares phase estimate by $\phi_{LS}(x, y, t) = -2\pi\text{OPD}(x, y, t)/\lambda$.

For the purposes of this work, 16 independent SHWFS measurements were the focus of the analysis. These data were collected at a sample rate of 200 Hz for 10 s. All of these measurements were taken the morning of 2023-07-10, eight of which were collected between 0750 and 0810 DST and the other eight were collected between 1115 and 1135 DST. As expected, the optical-turbulence conditions were much weaker during the early-morning collections compared with the late-morning collections. Example SHWFS imagery from these measurements is shown in Fig. 4. Here, the figure's color map was inverted such that the individual irradiance patterns are easier to see in print. Figure 4(a) shows an example SHWFS image collected in the early-morning data collection window and Fig. 4(b) shows an example SHWFS image collected in the late-morning data.

From these two example SHWFS frames, there are obvious differences in the measured irradiance patterns. In Fig. 4(a), the subaperture irradiance patterns all exhibit a similar shape and size. However, in Fig. 4(b), we see that many of the SHWFS subaperture irradiance patterns exhibit a large degree of beam spreading. This is particularly noticeable in the top-right and top-left portions of the frame. To use these measurements to calculate beam spread, a few additional processing steps need to be employed, namely, for each irradiance pattern, thresholding was used to eliminate residual ambient light from the AOI. Because ambient light drastically alters the local $D4\sigma$ calculations, this becomes a necessary step when performing beam-spread calculations. After doing so, a beam-spread threshold was imposed to determine which subapertures exhibited sufficient beam spreading to qualify for a branch-point identification. For the system parameters used in these data collections, a threshold value of $D4\sigma/D_{DL} = 1.3$ was used for the experimental data. In other words, if $D4\sigma$ was measured to be less than 1.3 times the diffraction-

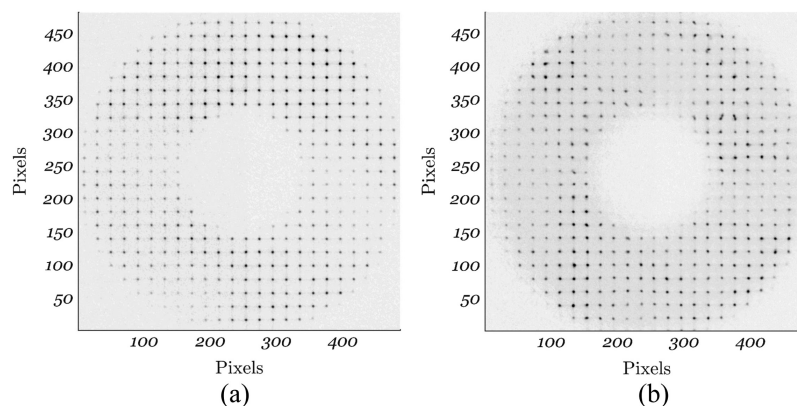


Fig. 4 (a) Example SHWFS frame collected during the early morning on 2023-07-10. (b) Example SHWFS frame collected during the late morning on 2023-07-10.

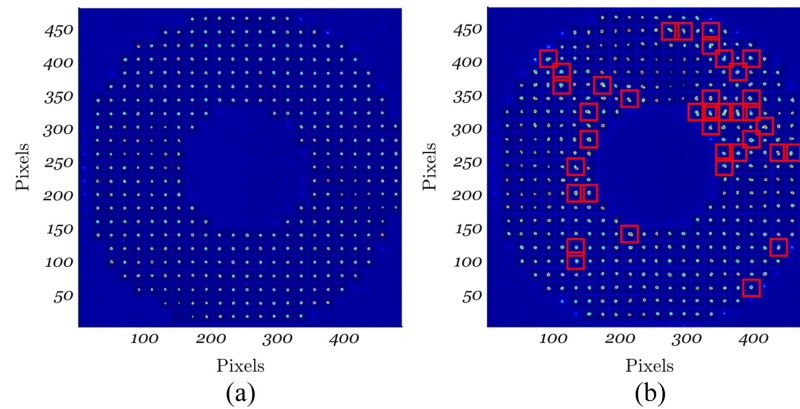


Fig. 5 (a) Processed SHWFS frame collected during the early morning on 2023-07-10. (b) Processed SHWFS frame collected during the late morning on 2023-07-10. Overlaid are red squares indicating subaperture locations where $D4\sigma/D_{DL}$ exceeded the threshold value.

limited spot size, it was said that there was no branch point present. However, if $D4\sigma$ was measured to be greater than 1.3 times the diffraction-limited spot size, it was said that there was a branch point present. After performing these additional data reduction steps, the processed version of the SHWFS images from Fig. 4 is shown in Fig. 5. Here, red squares were used to highlight AOIs in which the beam-spread approach determined that a branch point was present.

The processed SHWFS frame collected in the early morning is shown in Fig. 5(a). During this time, turbulence was weak and no branch points were detected using the beam-spread approach. The processed SHWFS frame collected in the late morning is shown in Fig. 5(b). Here, we see that many branch points were detected across the SHWFS frame with a grouping of detections in the top-right and top-left portions of the pupil. These measurements will be further analyzed and discussed in the next section.

4 Results and Discussion

The following sections present the branch-point identification results obtained using both wave-optics simulations and experimental data collections.

4.1 Simulation Results

As discussed in Sec. 3.1, due to the fine resolution of the complex-optical field afforded by simulation, Eq. (1) provided an excellent method for identifying the known branch-point locations. After which, the SHWFS model was applied to this complex-optical field to obtain simulated images. Subsequently, the beam spread and circulation of phase gradient approaches were employed, and the results were compared with the known branch-point locations. For the simulation data, the beam-spread and circulation of phase gradients thresholds were defined to be 1.75. These thresholds were selected with the goal of maximizing branch point detections while trying to minimize false-positive detections. At this point, these thresholds were determined heuristically. However, future work seeks to identify “rules of thumb” for selecting these threshold values.

A proximity metric, ϵ , was used to determine whether or not a branch point was correctly identified. Here, the known x and y branch-point locations (x_{KNOWN} and y_{KNOWN}), as well as the locations in which both approaches identified branch points (x_{ID} and y_{ID}), were recorded. Subsequently, for each detection, the distance to the closest actual branch point was calculated using

$$\epsilon = \sqrt{(x_{\text{ID}} - x_{\text{KNOWN}})^2 + (y_{\text{ID}} - y_{\text{KNOWN}})^2}. \quad (6)$$

A correct detection was recorded if an actual branch point was less than $\sqrt{2}d$ from a detection by the approaches described above. Otherwise, a false-positive detection was recorded.

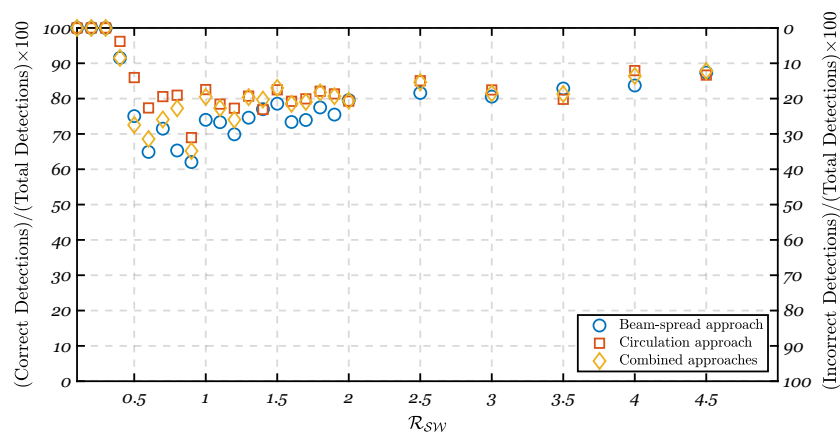


Fig. 6 Percent of correct and incorrect branch-point detections using the beam-spread, circulation of phase gradients, and combined identification approaches.

For the simulations discussed in Sec. 3.1, the known branch-point locations and the SHWFS-measured branch-point locations were calculated for each realization and each turbulence condition. The branch points identified using both approaches and the known branch-point locations were used to compute the proximity metric described in Eq. (6). Subsequently, the number of branch points correctly identified was compared with the total number of identifications. These results were then averaged across each turbulence condition and are plotted in Fig. 6. Here, the x axis is \mathcal{R}_{SW} and the left y axis is the percent of correct identifications. The blue circle markers represent the results obtained using the beam-spread approach, the red square markers represent the results obtained using the circulation of phase gradients approach, and the yellow diamond markers represent the results obtained using the combination of both approaches.

Using the thresholds described above, we see that both the beam-spread and circulation of phase gradients approaches performed similarly across all optical-turbulence conditions. Given these simulation parameters and thresholding values, the percent of correct identifications tended to approach 85% in high Rytov number conditions but never dropped below 60% correct identifications. When combining the branch points identified using both approaches, duplicate identifications were first removed. Because the beam-spread and circulation of phase gradients approaches performed similarly in terms of percentage of correct identifications, the combination of the two approaches also performed similarly. The percent of incorrect branch-point identifications, or false-positive identifications, is simply 100 minus the percent of correct identifications. For convenience, the percent of incorrect identifications is plotted on the right y axis of Fig. 6. These false-positive detections result from non-uniform illumination across the lenslet pupils (C-tilt/G-tilt anisoplanatism⁷), energetic optical aberrations smaller than the size of the lenslet pupil ($d/r_0 > 1$), and detector noise. Recognizing that false positives are to be expected, the thresholding parameters can be adjusted to change the performance. Specifically, larger thresholds limit the number of false-positive detections but also miss many branch points, whereas smaller thresholds identify many branch points at the cost of allowing for more false-positive detections. Reference 32 explored this trade space in earnest for the beam-spread approach. For the purposes of this paper, we focus on studying the relationship between the two methods for identifying branch points, recognizing however that different threshold values can be selected tailored toward one's goals. It is also worth noting that there is a “dip” in percentage of correct identifications for both the beam-spread and the circulation of phase gradients approaches between $\mathcal{R}_{SW} = 0.5 - 1.5$. It is believed that this behavior results from regions of strong destructive interference where branch points have not yet formed. For more information, see Ref. 32, where this behavior was first explored.

Figure 6 reveals the expected percentage of correct versus incorrect detections; however, those results do not reveal the identified number of branch points compared with the known number of branch points. To better summarize the simulated branch-point identification results, a few additional metrics were recorded. Specifically, the total number of correctly identified

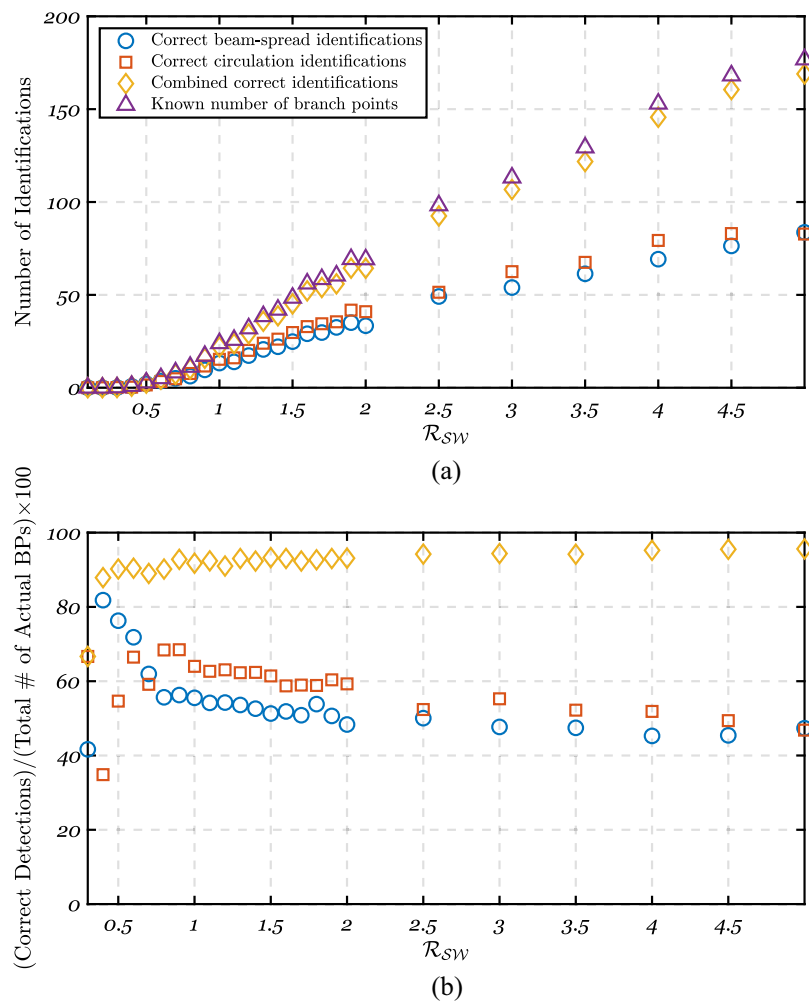


Fig. 7 (a) Correct number of branch-point detections. (b) Percentage of correct branch-point detections compared with the total number of known branch points.

branch points using the beam-spread approach, the total number of correctly identified branch points using the circulation of phase gradients approach, the total number of correctly identified branch points using both the beam spread and circulation of phase gradients approaches (with duplicate identifications removed), and the known number of branch points. Recall that the known number of branch point results was obtained using Eq. (1) on the complex-optical field before applying the SHWFS model. These statistics were calculated for each simulation iteration and then averaged over each simulated turbulence condition. The results are presented in Fig. 7. Here, the x -axis is the simulated \mathcal{R}_{SW} and the y -axis is the number of detections. The results in Fig. 7(a) are displayed as the number of branch points correctly identified and the results in Fig. 7(b) are displayed as the percent of correct detections compared with the known total number of branch points.

In Fig. 7, the results obtained using the beam-spread approach are represented using blue circle markers, the results obtained using the circulation of phase gradients approach are represented using red square markers, the results obtained using the correctly identified branch points from both the beam spread and circulation of phase gradients approaches are represented using yellow diamond markers, and the known number of branch points is represented using purple triangle markers. As expected, Fig. 7(a) reveals that branch points first begin to form for \mathcal{R}_{SW} between 0.2 and 0.3 and increase with increasing \mathcal{R}_{SW} thereafter. We see that for the thresholds described above, a similar number of branch points were correctly identified by both the circulation of phase gradients and the beam-spread approaches. However, the number of branch points correctly identified by both approaches is much less than the known number

of branch points across all optical-turbulence conditions. When the correct branch-point identifications from both approaches are combined, we see that the number of correct identifications is much closer to the known number of branch points. This is an encouraging result as it further substantiates the result presented in Fig. 2; namely, the two different approaches are sensitive to branch points located in different portions of the SHWFS lenslet pupils. As such, when both approaches are used together, a larger number of branch points are identified.

Results for a single realization of $\mathcal{R}_{SW} = 3.0$ optical-turbulence condition are plotted in Fig. 8. Here, Fig. 8(a) presents the calculated $D4\sigma/D_{DL}$, and Fig. 8(c) presents the calculated circulation of phase gradients. In both of these plots, the known branch-point locations are overlaid with black circle and square markers. The circle markers represent branch points of clockwise rotation and square markers represent branch points of counterclockwise rotation. From Fig. 8(a), it is clear that the known branch-point locations are densely packed near pupil locations with higher measured $D4\sigma/D_{DL}$ values. Similarly, in Fig. 8(c), known branch-point locations are also located where circulation values are higher. Here, positive circulation (yellow) indicates regions where clockwise circulation was detected, and negative circulation (blue) indicates regions where counterclockwise circulation was detected. Figures 8(b) and 8(d) show the flag matrices indicating where branch points were identified for both the beam-spread and circulation of phase gradient approaches, respectively. In both of these plots, yellow indicates locations where the algorithms identified branch points and blue represents subaperture locations where no branch points were identified. Green circles are plotted to indicate correct algorithm

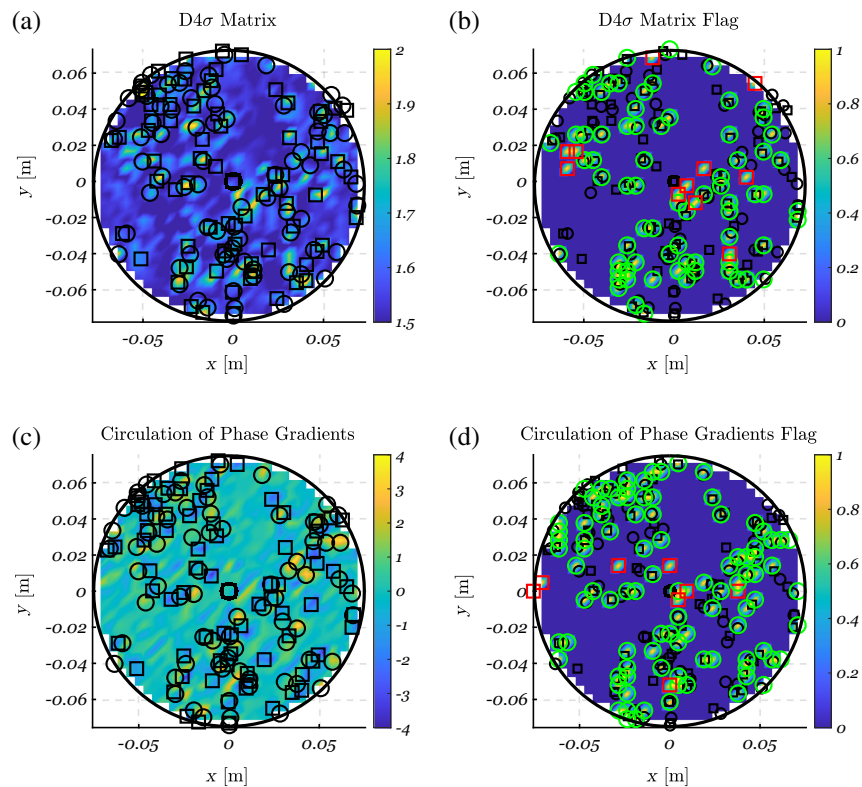


Fig. 8 (a) Calculated $D4\sigma/D_{DL}$ values from a simulated $\mathcal{R}_{SW} = 3.0$ optical-turbulence condition. The known branch-point locations are overlaid with black square and circle markers. (b) The flag matrix indicating where branch points were identified using the beam-spread approach. Correct branch-point identifications are plotted as green circles and incorrect branch-point identifications are plotted as red squares. (c) Calculated circulation of phase gradient values from a simulated $\mathcal{R}_{SW} = 3.0$ optical-turbulence condition. The known branch-point locations are overlaid with black square and circle markers. Here, the black-circle markers represent branch points of clockwise rotation and the black-square markers represent branch points of counterclockwise rotation. (d) Flag matrix indicating where branch points were identified using the circulation of phase gradients approach. Correct branch-point identifications are plotted as green circles and incorrect branch-point identifications are plotted as red squares.

detections and red squares are plotted to indicate false-positive detections. The known branch-point locations are also overlaid with black circle and square markers.

We see that both algorithms identified a large number of the total branch points present within the pupil; however, many locations of correct and incorrect branch-point identifications are not the same between both approaches. Specifically, there are many branch-point locations that were missed by one algorithm but identified by the other. From the results presented in Fig. 2, the different correct and missed branch-point identifications from the two algorithms shown in Fig. 8 are likely due to the different sensitivities of each algorithm to branch-point locations within an SHWFS lenslet pupil. Specifically, the beam-spread approach is better at detecting branch points toward the middle of the subapertures, whereas the circulation of phase gradients approach tends to do better when the branch point is located toward the edge of the subaperture.

4.2 Experimental Results

The results of the experiment described in Sec. 3.2.1 are discussed here. SHWFS measurements were collected and the processing procedures described in Sec. 3.2.2 were applied. For each SHWFS measurement, Eq. (2) was used to calculate the beam spread for each SHWFS irradiance pattern and measured SHWFS slopes were used to calculate the circulation of phase gradients using Eq. (1). Thresholds were applied to dictate the extent of beam spread or local circulation that was sufficient to qualify for a branch-point identification. For all experimental data, the beam-spread threshold was selected to be $D4\sigma/D_{DL} = 1.3$ and the circulation of phase gradients threshold was selected to be 2.0. Similar to the thresholds defined for the simulation data, these thresholds were heuristically selected. Future work seeks to establish concrete procedures for selecting both the beam-spread and circulation thresholds.

Figure 9 shows beam-spread and circulation of phase gradients results for a frame collected in the early morning. These results are associated with the SHWFS images shown in Figs. 4(a) and 5(a). Figure 9(a) presents the calculated $D4\sigma/D_{DL}$ values and Fig. 9(c) presents the calculated circulation of phase gradient values for this specific case. We see that both the calculated

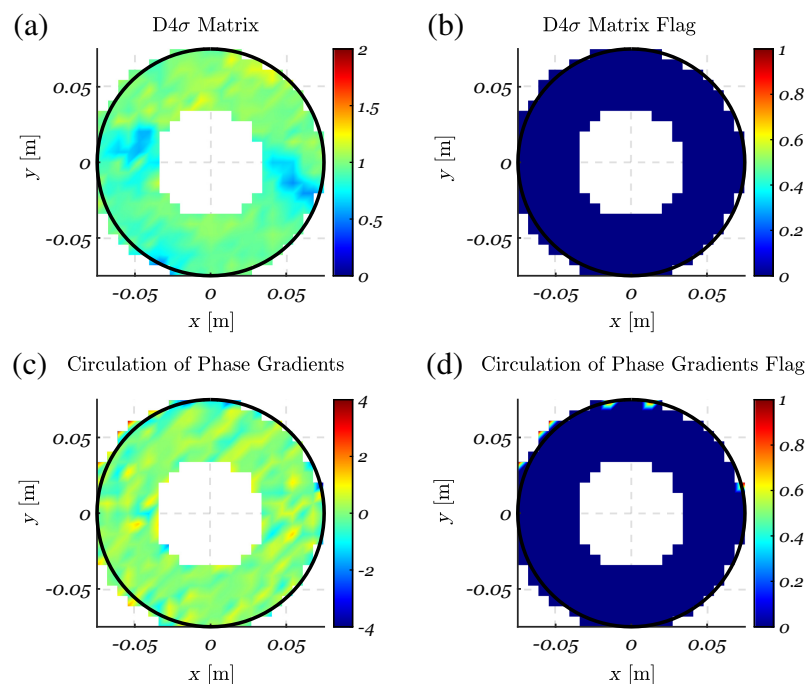


Fig. 9 (a) Calculated $D4\sigma/D_{DL}$ values from experimental data collected in the early morning. (b) Flag matrix indicating where branch points were identified using the beam-spread approach. (c) Calculated circulation of phase gradient values from experimental data collected in the early morning. (d) Flag matrix indicating where branch points were identified using the circulation of phase gradients approach.

beam spread and circulation of phase gradient values were low in amplitude across the entire pupil. As a result, no branch points were identified using the beam-spread approach as shown in Fig. 9(b). The circulation of phase gradients approach revealed a few identifications that were close to the edge of the aperture stop, as shown in Fig. 9(d). These identifications are likely associated with error due to the clipping of the AOI by the aperture stop rather than caused by turbulence-induced branch points.

Figure 10 presents the beam spread and circulation of phase gradients results for a frame collected in the late morning. These results are associated with the SHWFS images presented in Figs. 4(b) and 5(b). Similar to Fig. 9, Fig. 10(a) presents the calculated $D4\sigma/D_{DL}$ values and Fig. 10(c) presents the calculated circulation of phase gradients values. Unlike Fig. 9, we see that there are many locations of large amplitude beam spread and circulation across the pupils. As described in Sec. 4.1, the positive and negative regions of the circulation of phase gradients plot represent branch-point identifications of opposite helicity. Here, positive circulation (red) indicates regions where clockwise circulation was detected and negative circulation (blue) indicates regions where counterclockwise circulation was detected. Recall that the beam-spread metric is normalized by the diffraction-limited spot size, i.e., $D4\sigma/D_{DL}$. As such, the calculated $D4\sigma/D_{DL}$ should never be less than one. However, as shown in Fig. 10(a), there are locations within the pupil where $D4\sigma/D_{DL} < 1$. This is not physical but is an artifact of imperfect thresholding of the individual irradiance patterns, as demonstrated in Fig. 5. The flagged branch-point identifications from both the beam-spread approach and the circulation of phase gradients approach are shown in Figs. 10(b) and 10(d), respectively. We see that both approaches reveal branch-point identifications in the top-right and left to top-left portions of the measurement pupil.

The number of branch-point identifications for each data collection is summarized and presented in Fig. 11(a). For each SHWFS collection, these statistics were calculated on a frame by frame basis and then averaged across all frames. Here, the x -axis is the SHWFS collection number and the y -axis is the number of detections. Recall that data collections 1 to 8 were collected in the early morning, and data collections 9 to 16 were collected in the late morning. Similar to Fig. 7, the number of branch points identified using the beam-spread approach is represented using blue circle markers, the number of branch points identified using the circulation of phase

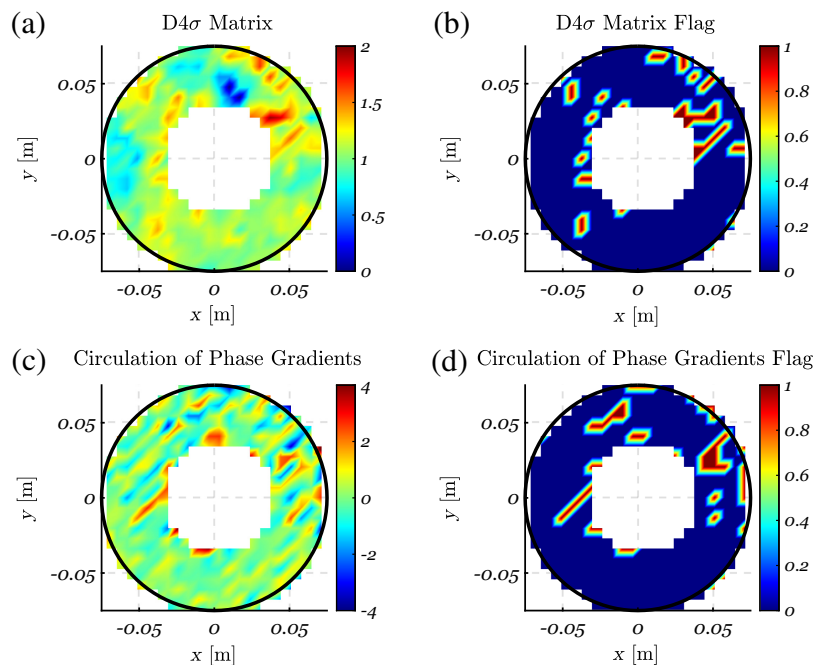


Fig. 10 (a) Calculated $D4\sigma/D_{DL}$ values from experimental data collected in the late morning. (b) Flag matrix indicating where branch points were identified using the beam-spread approach. (c) Calculated circulation of phase gradient values from experimental data collected in the late morning. (d) Flag matrix indicating where branch points were identified using the circulation of phase gradients approach.

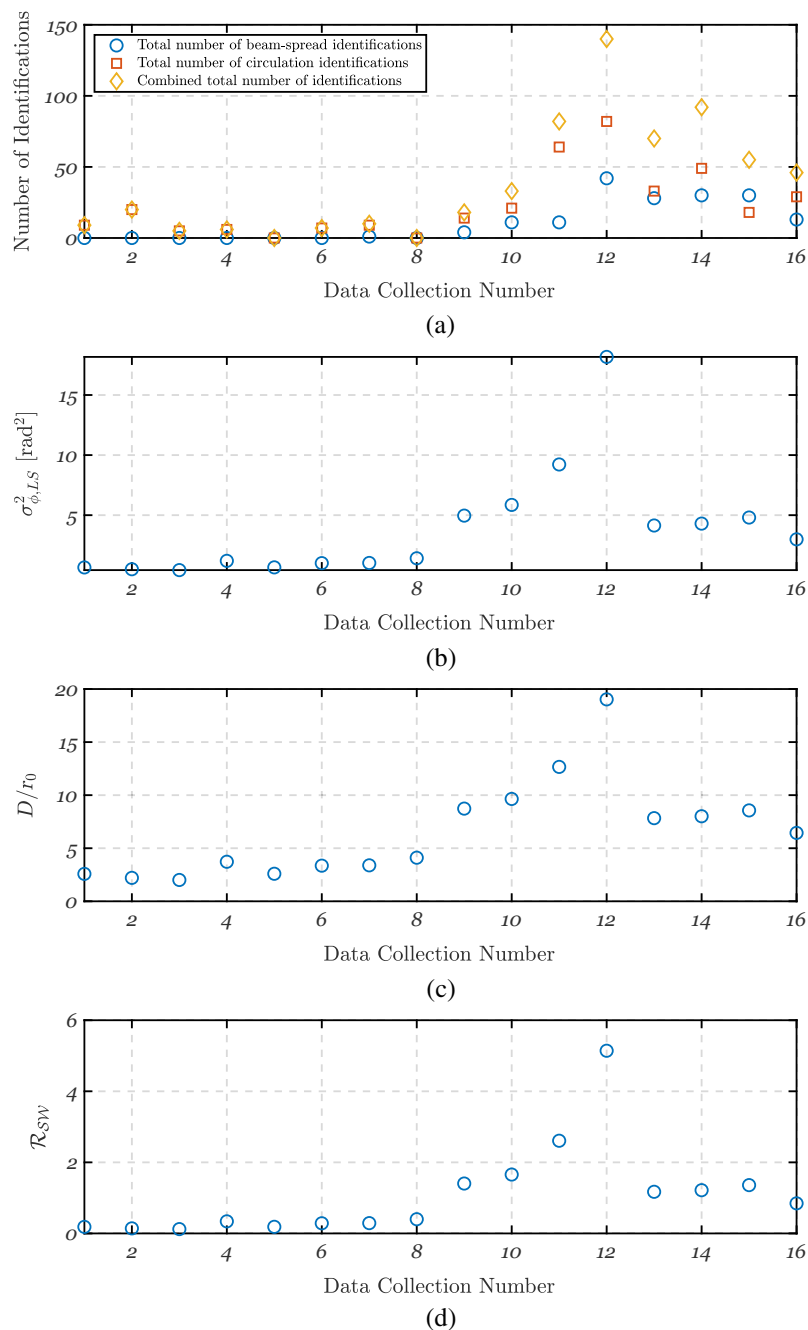


Fig. 11 (a) Number of branch-point detections. (b) Calculated least-squares phase variance. (c) D/r_0 estimated using the least-squares, tilt-removed phase variance. (d) \mathcal{R}_{SW} estimated using the measured r_0 values.

gradients approach is represented using red square markers, and the number of branch points identified using both the beam spread and circulation of phase gradients approaches is represented using yellow diamond markers. As expected, the low turbulence conditions seen in the early morning resulted in few to no branch-point detections. Conversely, the stronger optical-turbulence environment in the late-morning led to many branch-point detections. We also see that using either the beam spread or the circulation of phase gradients approaches alone produced much fewer detections than the number of combined detections. Because these results were obtained experimentally, we do not definitively know the true total number of branch points. As such, we expect that some of these identifications are associated with false-positive detections. Nevertheless, the trends observed in this plot are similar to those shown in Fig. 7. It should

also be noted that more meaningful experimental results could be gleaned with a larger number of data collections as well as longer duration data collections (>10 s). This will be the focus of future work.

In addition to studying the branch-point detection techniques discussed in this paper, the SHWFS slopes were used in a least-squares reconstructor to estimate the continuous OPD(x, y, t) aberration. After removing the tip, tilt, piston, and lensing aberrations from the reconstructed OPD(x, y, t) field, the OPD_{RMS} was calculated by taking the root-mean-square over the spatial dimension and temporally averaging for each data point. Subsequently, the OPD_{RMS} calculated for each data collection was used to calculate the least-squares phase variance as, $\sigma_{\phi,LS}^2 = [-2\pi\text{OPD}_{\text{RMS}}/\lambda]^2$. These results are presented in Fig. 11(b). Comparing Figs. 11(a) and 11(b), we see that there are more branch-point identifications when a higher least-squares phase variance was measured. Although these results coincide with intuition, it is encouraging to see this relationship.

Recognizing that r_0 is related to the variance of optical quantities related to phase, the least-squares phase variance, presented in Fig. 11(b), can be used to compute r_0 through the relation $\sigma_{\phi,LS}^2 = 0.134(D/r_0)^{5/3}$.⁵² In this expression, $\sigma_{\phi,LS}^2$ assumes that the tip, tilt, and piston are removed, as was the case in the reconstructed OPD(x, y, t). The resultant r_0 values calculated using this expression are normalized by D and presented in Fig. 11(c). Here, we see that D/r_0 varied between approximately $D/r_0 = 2 - 4$ for the data collected in the early morning. Conversely, D/r_0 primarily varied between ~ 6 and 13 for the data collected in the late morning. Data collection number 12 was a clear outlier with an approximate calculated D/r_0 of 19. From Fig. 11(a), significantly more branch points were also identified for this data point.

By assuming uniform turbulence strength along the propagation path, the r_0 values calculated and presented in Fig. 11(c) were used to estimate C_n^2 via Eq. (4). Subsequently, these C_n^2 estimates were then used to estimate \mathcal{R}_{SW} using Eq. (3); the results of which are presented in Fig. 11(d). We see that for the data collected in the early morning, \mathcal{R}_{SW} varied between 0.1 and 0.4. For the data collected in the late-morning, \mathcal{R}_{SW} primarily varied between 0.9 and 2.6 with the outlier at data collection number 12 resulting in a \mathcal{R}_{SW} of 5.14.

5 Conclusions

In this paper, two methods for identifying branch points from SHWFS measurements were studied: the circulation of phase gradients approach and the beam-spread approach. Although the circulation of phase gradients is considered the “tried and true,” the beam-spread approach was recently introduced and shows promise. The performance of these two algorithms was first assessed using an idealized optical-vortex model. Here, the optical-vortex was advected across the measurement pupil to investigate how both algorithms respond as a function of branch-point location. It was found that these two approaches are synergistic. In other words, the beam-spread approach works best when the branch point is located toward the center of the lenslet pupil, whereas the circulation of phase gradients approach works best when the branch point is located toward the edge of the lenslet pupil.

Wave-optics simulations were also used to study both approaches under varying optical-turbulence conditions. Because branch-point locations are known in simulation, the performance of both approaches could be assessed. For the selected thresholds, it was found that both approaches correctly identified branch points from 60% to 85% of the time across the range of optical-turbulence conditions studied. It was also shown that by combining the branch points correctly identified by both approaches, the total number of correctly identified branch points was much closer to the known number of branch points compared with using either approach alone. This result further validates the same synergistic behavior observed with the idealized optical-vortex model.

Experimental SHWFS measurements of a beam that propagated approximately 2.4 km through a littoral test environment were also collected. The analysis presented in this paper was focused on eight data points collected in the early morning and eight data points collected in the late morning. As expected, optical-turbulence conditions were fairly benign in the early morning leading to few to no branch-point detections. However, turbulence conditions changed markedly by the late morning and an appreciable number of branch points were identified by both algorithms. Despite not having known branch-point locations in the experiment, the combination of

the two branch-point identification approaches led us to believe that the same synergistic behavior observed with the simple optical-vortex model and in wave-optics simulations was observed in the experiment.

In conclusion, the combination of the circulation of phase gradients approach in conjunction with the beam-spread approach shows promise for the collective improvement of branch-point identification from SHWFS measurements; the likes of which may help researchers better study optical-turbulence environments or develop novel branch-point-tolerant phase reconstruction algorithms from SHWFS measurements.

Disclosures

The U.S. Government is authorized to reproduce and distribute reprints for governmental purposes notwithstanding any copyright notation thereon.

Distribution Statement A. Approved for public release: distribution is unlimited. Public Affairs release approval #: NSWCCD-PN-23-00197.

Code and Data Availability

The data that support the findings of this article are not publicly available. They can be requested from the author using the email address provided above.

Acknowledgments

Grateful acknowledgement is given to ONR; their sponsorship and continuing guidance of the IAR program has made this research possible. These efforts were funded under ONR award N0001423WX00073.

References

1. M. F. Spencer, "Limitations of the deep-turbulence problem," in *Imaging and Appl. Opt. Congr.*, OSA Technical Digest (2021).
2. D. L. Fried, "Branch point problem in adaptive optics," *J. Opt. Soc. Am.* **15**, 2759 (1998).
3. D. W. Oesch, D. J. Sanchez, and C. L. Matson, "The aggregate behavior of branch points: measuring the number and velocity of atmospheric turbulence layers," *Opt. Express* **18**, 22377 (2010).
4. D. W. Oesch, D. J. Sanchez, and C. M. Tewksbury-Christle, "Aggregate behavior of branch points – persistent pairs," *Opt. Express* **20**, 1046 (2012).
5. D. L. Fried and J. L. Vaughn, "Branch cuts in the phase function," *Appl. Opt.* **31**, 2865 (1992).
6. J. D. Barchers, D. L. Fried, and D. J. Link, "Evaluation of the performance of a shearing interferometer in strong scintillation in the absence of additive measurement noise," *Appl. Opt.* **41**, 3674 (2002).
7. J. D. Barchers et al., "Performance of wavefront sensors in strong scintillation," *Proc. SPIE* **4839**, 217–227 (2003).
8. J. D. Barchers, D. L. Fried, and D. J. Link, "Evaluation of the performance of hartmann sensors in strong scintillation," *Appl. Opt.* **41**, 1012 (2002).
9. M. T. Banet and M. F. Spencer, "Compensated-beacon adaptive optics using least-squares phase reconstruction," *Opt. Express* **28**, 36902 (2020).
10. M. C. Roggemann and A. C. Koivunen, "Wave-front sensing and deformable-mirror control in strong scintillation," *J. Opt. Soc. Am. A* **17**, 911 (2000).
11. M. F. Spencer and S. J. Cusumano, "Impact of branch points in adaptive optics compensation of thermal blooming and turbulence," *Proc. SPIE* **8165**, 816503 (2011).
12. M. F. Spencer, "Wave-optics investigation of turbulence thermal blooming interaction: I. Using steady-state simulations," *Opt. Eng.* **59**(8), 081804 (2020).
13. M. F. Spencer, "Wave-optics investigation of turbulence thermal blooming interaction: II. Using time-dependent simulations," *Opt. Eng.* **59**(8), 081805 (2020).
14. M. F. Spencer and T. J. Brennan, "Deep-turbulence phase compensation using tiled arrays," *Opt. Express* **30**, 33739–33755 (2022).
15. D. Oesh, "The aggregate behavior of branch points - branch point density as a characteristic of an atmospheric turbulence simulator," tech. rep., AFRL-RD-PS TP-2010-1010 (2009).
16. D. W. Oesch and D. J. Sanchez, "Photonic orbital angular momentum in starlight," *Astron. Astrophys.* **567**, A114 (2014).
17. D. W. Oesch et al., "The aggregate behavior of branch points: altitude and strength of atmospheric turbulence layers," *Proc. SPIE* **7816**, 781605 (2010).

18. D. W. Oesch et al., “The aggregate behavior of branch points: verification in wave optical simulation I,” *Proc. SPIE* **8380**, 83800O (2012).
19. D. W. Oesch et al., “The aggregate behavior of branch points: verification in wave optical simulation II,” *Proc. SPIE* **8520**, 852003 (2012).
20. D. W. Oesch et al., “Aggregate behavior of branch points: characterization in wave optical simulation,” *Opt. Eng.* **51**, 106001 (2012).
21. D. J. Sanchez and D. W. Oesch, “The aggregate behavior of branch points: the creation and evolution of branch points,” *Proc. SPIE* **7466**, 746605 (2009).
22. D. J. Sanchez et al., “The aggregate behavior of branch points: a proposal for an atmospheric turbulence layer sensor,” *Proc. SPIE* **7816**, 781606 (2010).
23. D. J. Sanchez, D. W. Oesch, and P. R. Kelly, “The aggregate behavior of branch points: theoretical calculation of branch point velocity,” *Proc. SPIE* **8380**, 83800P (2012).
24. D. J. Sanchez and D. W. Oesch, “Hiding the phase: the filling of the slope discrepancy hilbert space,” *Proc. SPIE* **8520**, 852004 (2012).
25. J. R. Beck et al., “Wave-optics investigation of branch-point density,” *Opt. Eng.* **61**, 044104 (2022).
26. V. V. Voitsekhovich, D. Kouznetsov, and D. K. Morozov, “Density of turbulence-induced phase dislocations,” *Appl. Opt.* **37**, 4525 (1998).
27. M. Kalensky et al., “Estimation of atmospheric optical turbulence strength in realistic airborne environments,” *Appl. Opt.* **61**, 6268 (2022).
28. D. Fried, “Least-square fitting a wave-front distortion estimate to an array of phase-difference measurements,” *J. Opt. Soc. Am.* **67**, 370–375 (1977).
29. R. Hudgin, “Wave-front reconstruction for compensated imaging,” *J. Opt. Soc. Am.* **67**, 375–378 (1977).
30. W. H. Southwell, “Wave-front estimation from wave-front slope measurements,” *J. Opt. Soc. Am.* **70**(8), 998–1006 (1980).
31. P. Merritt and M. Spencer, *Beam Control for Laser Systems*, Directed Energy Professional Society, High Energy Laser Joint Technology Office, Albuquerque, New Mexico (2018).
32. M. Kalensky, “Branch-point identification using second-moment Shack–Hartmann wavefront sensor statistics,” *Appl. Opt.* **62**, G101–G111 (2023).
33. M. Kalensky et al., “Branch-point detection using a Shack–Hartmann wavefront sensor,” *Proc. SPIE* **12693**, 126930C (2023).
34. G. A. Tyler, “Reconstruction and assessment of the least-squares and slope discrepancy components of the phase,” *J. Opt. Soc. Am.* **17**, 1828 (2000).
35. K. Murphy, R. Mackey, and C. Dainty, “Branch point detection and correction using the branch point potential method,” *Proc. SPIE* **6951**, 695105 (2008).
36. M. Chen, F. S. Roux, and J. C. Olivier, “Detection of phase singularities with a Shack–Hartmann wavefront sensor,” *J. Opt. Soc. Am. A* **24**, 1994 (2007).
37. M. Chen and F. S. Roux, “Dipole influence on Shack–Hartmann vortex detection in scintillated beams,” *J. Opt. Soc. Am. A* **25**, 1084 (2008).
38. W. J. Wild and E. O. L. Bigot, “Rapid and robust detection of branch points from wave-front gradients,” *Opt. Lett.* **24**, 190 (1999).
39. J. Goodman, *Introduction to Fourier Optics*, W. H. Freeman & Co (2017).
40. A. E. Siegman, “How to (maybe) measure laser beam quality,” in *DPSS (Diode Pumped Solid State) Lasers: Appl. and Issues*, OSA (1998).
41. M. Kalensky, M. R. Kemnetz, and M. F. Spencer, “Effects of shock waves on Shack–Hartmann wavefront sensor data,” *AIAA J.* **61**, 2356–2368 (2023).
42. M. Kalensky, “Airborne measurement of atmospheric-induced beam jitter,” PhD thesis, University of Notre Dame (2022).
43. M. Kalensky, M. R. Kemnetz, and M. F. Spencer, “Effects of shock-related discontinuities on SHWFS measurements: modeling and simulation,” *Proc. SPIE* **12239**, 122390J (2022).
44. J. Schmidt, *Numerical Simulation of Optical Wave Propagation with Examples in MATLAB*, SPIE Press, Bellingham, Washington (2010).
45. J. M. Martin and S. M. Flatté, “Intensity images and statistics from numerical simulation of wave propagation in 3-D random media,” *Appl. Opt.* **27**, 2111 (1988).
46. J. M. Martin and S. M. Flatté, “Simulation of point-source scintillation through three-dimensional random media,” *J. Opt. Soc. Am.* **7**, 838 (1990).
47. D. Knepp, “Multiple phase-screen calculation of the temporal behavior of stochastic waves,” *Proc. IEEE* **71**(6), 722–737 (1983).
48. C. Macaskill and T. E. Ewart, “Computer simulation of two-dimensional random wave propagation,” *IMA J. Appl. Math.* **33**(1), 1–15 (1984).
49. M. Roggemann, *Imaging Through Turbulence*, CRC Press, Boca Raton (1996).

50. E. Bates, J. Z. Karlovich, and W. L. Filkoski, "Year-long atmospheric characterization effort for laser weapon testing on the Potomac River Test Range (PRTR) at the Naval Surface Warfare Center Dahlgren Division (NSWCDD)," *Opt. Eng.* **61**, 076105 (2022).
51. T. J. Bukowski et al., "Optical-turbulence characterization of a littoral test environment using a Shack-Hartmann wavefront sensor," *Proc. SPIE* **12693**, 126930Q (2023).
52. R. J. Noll, "Zernike polynomials and atmospheric turbulence," *J. Opt. Soc. Am.* **66**, 207 (1976).

Matthew Kalensky is an engineer at the Naval Surface Warfare Center Dahlgren Division. He received his BS degree in mechanical and materials engineering from Loyola University Maryland in 2017 and his MS degree and PhD in aerospace engineering from the University of Notre Dame in 2020 and 2022, respectively. He actively runs a cross-service adaptive-optics working group; is a chair for the Unconventional Imaging, Sensing, and Adaptive Optics conference at SPIE Optics and Photonics; and is the Webinar Officer for the Optica's Laser System's Technical Group. His expertise and research interests are in beam control, deep-turbulence characterization, and aero effects.

Denis W. Oesch received his PhD in astrophysics from the New Mexico Institute of Mining and Technology in 2005. He has been working for Leidos for the past 19 years in adaptive optics and atmospheric characterization. He splits his time supporting Air Force Research Laboratory projects at the Starfire Optical Range, Beam Control Laboratory and the Environmental Laser Test Facility, Kirtland Air Force Base, New Mexico.

Timothy J. Bukowski is a current graduate student in the Aero-Optics group at the University of Notre Dame, where he works on many problems related to laser propagation systems. He was also an SSEP intern at the Naval Surface Warfare Center Dahlgren Division within the Integrated Engagement Systems Department and the Optics and Beam Control Branch, where he worked on problems related to beam propagation through distributed-volume turbulence. He is an Arthur J. Schmitt Leadership Fellow and was recently awarded the NDSEG fellowship.

Kelsey Miller is an optical scientist at Naval Surface Warfare Center Dahlgren Division (NSWCDD). She received her bachelor's degree in astrophysics from New Mexico Tech and her master's degree and PhD in optical sciences from the University of Arizona College of Optical Science. She has served as the lab PI of AFRL RDL's Beam Control Lab and is now a beam control subject matter expert at NSWCDD.

Darren Getts is a scientist at the Naval Surface Warfare Center Dahlgren Division. He received his BS degree from the University of Mary Washington with a double major in physics (honors) and mathematics. He received his MS degree in applied physics from Johns Hopkins University. He actively researches atmospheric effects on propagating optical waves through theory and experimental design.